Low-Frequency Variability in Shallow-Water Models of the Wind-Driven Ocean Circulation. Part I: Steady-State Solution*

ERIC SIMONNET+

Laboratoire de Mathématiques, Université Paris-Sud, Orsay, France

MICHAEL GHIL# AND KAYO IDE

Department of Atmospheric Sciences, and Institute of Geophysics and Planetary Physics, University of California, Los Angeles, Los Angeles, California

ROGER TEMAM

Laboratoire de Mathématiques, Université Paris-Sud, Orsay, France, and Department of Mathematics, Indiana University, Bloomington, Indiana

SHOUHONG WANG

Department of Mathematics, Indiana University, Bloomington, Indiana

(Manuscript received 12 March 2001, in final form 19 September 2002)

ABSTRACT

Successive bifurcations—from steady states through periodic to aperiodic solutions—are studied in a shallow-water, reduced-gravity, 2½-layer model of the midlatitude ocean circulation subject to time-independent wind stress. The bifurcation sequence is studied in detail for a rectangular basin with an idealized spatial pattern of wind stress. The aperiodic behavior is studied also in a North Atlantic–shaped basin with realistic continental contours. The bifurcation sequence in the rectangular basin is studied in Part I, the present article. It follows essentially the one reported for single-layer quasigeostrophic and 1½-layer shallow-water models. As the intensity of the north–south-symmetric, zonal wind stress is increased, the nearly symmetric double-gyre circulation is destabilized through a perturbed pitchfork bifurcation. The low-stress steady solution, with its nearly equal subtropical and subpolar gyres, is replaced by an approximately mirror-symmetric pair of stable equilibria. The two solution branches so obtained are named after the inertial recirculation cell that is stronger, subtropical or subpolar, respectively. This perturbed pitchfork bifurcation and the associated Hopf bifurcations are robust to changes in the interface friction between the two active layers and the thickness H_2 of the lower active layer. They persist in the presence of asymmetries in the wind stress and of changes in the model's spatial resolution and finite-difference scheme. Time-dependent model behavior in the rectangular basin, as well as in the more realistic, North Atlantic–shaped one, is studied in Part II.

1. Introduction and motivation

The main motivation of this study is to understand the low-frequency variability of the large-scale midlatitude ocean circulation. We concentrate on the wind-driven double-gyre circulation formed by the subtropical anticyclonic gyre and the subpolar cyclonic gyre. Various spatial patterns of such a double-gyre circulation are observed in the midlatitude ocean basins of both hemispheres. This circulation contributes to the transport of heat and mass between low and high latitudes, and is believed to be an important source of interannual variability of the earth's climate (Speich and Ghil 1994; Meacham 2000). This has motivated an intensive study of the double-gyre circulation's properties, following Jiang et al. (1993, 1995) and Cessi and Ierley (1995). The main driving force for this ocean circulation is the wind stress that is characterized by a midlatitude zonal wind maximum and adjacent minima equatorward and

* Institute of Geophysics and Planetary Physics Publication Number 5743.

+ Current affiliation: Institut Non-Linéaire de Nice, Valbonne, France.

Current affiliation: Ecole Normale Supérieure, LMD, CNRS, Paris, France.

Corresponding author address: Dr. Eric Simonnet, Institut Non-Linéaire de Nice (INLN), UMR 6618, CNRS 1361, route des Lucioles, 06560 Valbonne, France.
E-mail: eric.simonnet@inln.cnrs.fr

poleward. Low-frequency, subannual, and interannual oscillations have been documented for time-independent wind stress in a variety of models and their physical causes are starting to be understood (Meacham 2000; Chang et al. 2001; Simonnet and Dijkstra 2002).

To study in greater depth the mechanisms of the double-gyre ocean circulation's low-frequency variability, we use a two-step approach. First, numerical bifurcation tools are applied to a rectangular ocean basin that corresponds roughly in size to that portion of the North Atlantic where nonlinear, advective processes are most active. Second, we examine the details of the behavior obtained in the rectangular basin in a more realistic model of the North Atlantic, using ETOPO-5 (earth topography-5 minute) bathymetry. The model we adopt for both geometries is a 2½-layer wind-driven, shallow-water (SW) model. The wind stress used in the rectangular basin is idealized, while in the more realistic geometry we use both an idealized and an observations-based wind stress (Hellerman and Rosenstein 1983).

Many authors have studied the effects of nonlinearity on the wind-driven ocean circulation. Veronis (1963, 1966) was the first to analyze multiple steady states and transitions to periodic solutions in the subtropical wind-driven gyre. Bryan (1963) noted transition to time-dependent behavior of a quasigeostrophic (QG) model for time-independent wind stress. Jiang et al. (1995) provided a preliminary bifurcation diagram for a wind-driven, double-gyre, SW model that led from multiple steady states through periodic solutions to aperiodic behavior. More recently, Berloff and Meacham (1997, 1998) and Meacham and Berloff (1997) studied the bifurcation structure of wind-driven, single- and multilayer, QG models for a small midlatitude ocean basin; both the single-gyre and double-gyre circulations were carefully examined. Fairly complete reviews appear in Pedlosky (1996), Meacham (2000), and Ghil et al. (2002b), while Chang et al. (2001) emphasize the similarities and differences between the single-gyre and double-gyre results.

In the present article, we study a 2½-layer wind-driven SW model and pay special attention to the dynamics of the circulation in the two active layers, as well as to the effect of the lower layer on the upper layer's double-gyre circulation. More precisely, the bifurcation structure of the 2½-layer SW model is numerically investigated using a (pseudo arclength) continuation method (Keller 1977; Legras and Ghil 1985; Speich et al. 1995; Dijkstra and Katsman 1997; Primeau 1998) along the bifurcated branches. The main driving force is the wind stress acting on the top layer.

When varying bifurcation parameters such as the strength σ of the wind stress, the interface friction parameter μ_1 or the reference thickness of the lower layer H_2, the flow undergoes a perturbed pitchfork bifurcation that leads from a unique steady state to the appearance of multiple steady states. This is followed by a Hopf bifurcation and the appearance of periodic solutions, followed in turn by that of quasi-periodic and chaotic solutions.

The main results of our study include

1) the robustness of the perturbed pitchfork bifurcation to the model's spatial resolution and the asymmetry in the forcing wind profile,
2) the role of barotropic and baroclinic instabilities in the successive Hopf bifurcations that lead to periodic and quasi-periodic behavior,
3) the role of homoclinic bifurcations in generating the low-frequency variability, and
4) the low-frequency behavior of our model in more realistic configurations.

Our study has two parts. The remarkable robustness of the perturbed pitchfork bifurcation is an important result of Part I. Equally robust is the ordering of the baroclinic and barotropic instabilities, with or without interfacial friction. The detailed study of the first global bifurcation that leads to the appearance of a homoclinic orbit is clearly an important step in understanding the low-frequency variability of the wind-driven circulation. It is especially new in the context of a multilayer SW model, where the symmetry is perturbed, and is a key result of Part II (Simonnet et al. 2003); so is the comparison between the observed low-frequency variability and the North Atlantic basin simulation.

The two parts are organized as follows. In section 2 of Part I, the present paper, we derive the equations for a 2½-layer SW model of the double-gyre wind-driven ocean circulation in a rectangular midlatitude basin. Similarities and differences between this model and a QG model are also discussed. In section 3, we briefly describe the numerical methods used in this study. In section 4, we show the basic bifurcation structure associated with the flow in the rectangular basin as the wind stress forcing increases. The dependence of this bifurcation structure on other parameters and on the model's spatial resolution is investigated in section 5. The results of Part I are summarized in section 6.

Part II (Simonnet et al. 2003) starts with a brief introduction and recapitulation of Part I. Its section 2 is devoted to the study of the Hopf bifurcations that lead to limit cycles in the rectangular-basin version of the model. In section 3, we then describe the transitions to aperiodic behavior as well as the phenomenology of low-frequency variability. This variability is also examined in section 4 for a geometry and wind stress that approximate fairly closely the North Atlantic basin. Concluding remarks for the entire study follow in section 5. Preliminary results of this investigation were reported by Simonnet (1998) and Simonnet et al. (1998).

2. Model formulation

The dynamical behavior of the midlatitude upper ocean is often described by reduced-gravity models, where one or several active layers lie above a motionless

layer of infinite depth. Thus, an n½-layer model describes an upper ocean with n distinct active layers; the ½ refers to the infinitely deep, quiescent layer. The fast barotropic gravity wave mode presents a severe burden for numerical models since it imposes a short time step of integration when using explicit schemes. By allowing the lower layer to be infinitely deep, the barotropic mode is removed and the first baroclinic mode of the system is now modeled as mathematically equivalent to the barotropic mode (see Gill 1982).

a. Governing equations

The basic hypothesis of SW models is to assume that the upper active layers are vertically homogeneous and hydrostatic. When a QG approximation is made, one has the possibility of deriving equations that are much simpler than the full SW equations, for example, the equivalent barotropic model (McCalpin and Haidvogel 1996; Berloff and Meacham 1997); as well as two- or multilayer QG equations (e.g., Pedlosky 1987; Dijkstra and Katsman 1997; Berloff and Meacham 1998). Rigorous mathematical results are easier to obtain for these models (see Wolanski 1989; Buffoni and Griffa 1990; Wang 1992; Wolanski and Ghil 1995, 1996, 1998); moreover, they are numerically much easier to solve.

Multilayer SW models, on the other hand, are closer in mathematical and numerical structure to the primitive-equation models that are being used more and more to study the general circulation of the atmosphere and oceans. In particular, SW models have been used to develop data assimilation methods for oceanographic problems (Jiang and Ghil 1993, 1997). This has motivated, at least in part, our choice of the 2½-layer SW models here, as a step in the direction of greater realism in the investigation of the double-gyre circulation's low-frequency variability.

Recent studies (Speich et al. 1995) demonstrated the possibility of computing numerically the branching structure of the SW equations, too, although theoretical bifurcation results are still missing. The dynamical behavior of SW and QG models exhibits striking similarities, at least when the nonlinearity is not too strong. Reduced-gravity SW models represent therewith a useful intermediate step in the modeling hierarchy (Ghil and Robertson 2000) between QG and general circulations models (GCMs) of the ocean. Genuine multilayer SW models with layers of finite depth are also been used. They seem to be less stable than reduced-gravity ones in general but exhibit very similar dynamical features including similar branches of solutions, oscillatory modes, and global bifurcations (see Nauw and Dijkstra 2001).

Shallow-water models are also used in other contexts than the midlatitude ocean circulation, such as the dynamics of the Great Red Spot and the Jovian atmosphere (Dowling 1995), as well as in theoretical studies of atmospheric low-frequency variability (Keppenne et al. 2000).

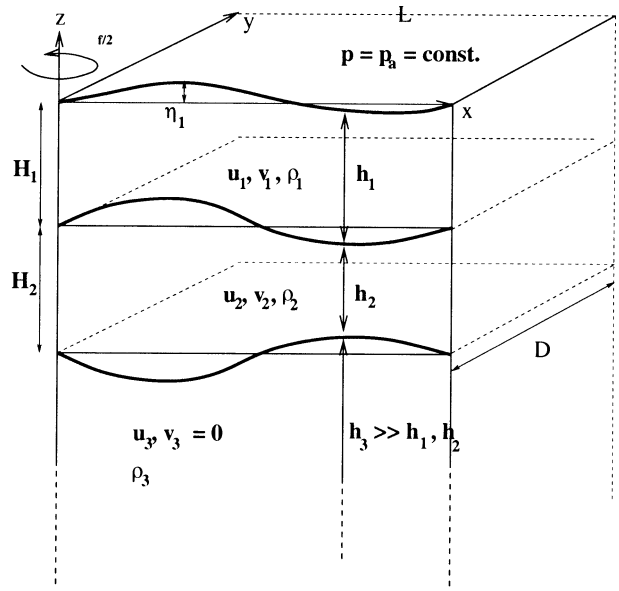

FIG. 1. Schematic diagram of the 2½-layer upper-ocean model.

Neglecting thermodynamics and outcropping of the thermocline, we consider here a 2½-layer SW model driven by a steady wind stress in a closed rectangular basin $\Omega = \{0 \le x \le L, 0 \le y \le D\}$. A more realistic geometry, approximating the North Atlantic basin, is also considered in Part II, section 4b. Contrary to the earlier 1½-layer SW models of Ghil and colleagues (Jiang et al. 1993, 1995; Speich et al. 1995), this model takes into account the possible occurrence of baroclinic instability processes. The 2½-layer model consists of two active layers of constant density ρ_1 and ρ_2 overlying an infinitely deep and quiescent layer of density ρ_3 (see Fig. 1).

The midlatitude oceans are often described in Cartesian coordinates (x, y, z) using the β-plane approximation (Gill 1982; Pedlosky 1987), where the Coriolis parameter is f given by $f_0 + \beta_0 y$. Integrating vertically the Navier–Stokes equations over the three layers and using the hydrostatic assumption for each layer, we derive the following governing partial differential equations (PDEs):

$$\frac{\partial U_1}{\partial t} + \nabla \cdot (U_1 \mathbf{V}_1) = -g_1 h_1 \frac{\partial h_1}{\partial x} - g_2 h_1 \frac{\partial h_2}{\partial x} + (f_0 + \beta_0 y) V_1 + A \Delta U_1 - R_1 (U_1 - U_2) + \frac{\tau^x}{\rho_1},$$

$$\frac{\partial V_1}{\partial t} + \nabla \cdot (V_1 \mathbf{V}_1) = -g_1 h_1 \frac{\partial h_1}{\partial y} - g_2 h_1 \frac{\partial h_2}{\partial y} - (f_0 + \beta_0 y) U_1 + A \Delta V_1 - R_1 (V_1 - V_2),$$

$$\frac{\partial h_1}{\partial t} = -\frac{\partial U_1}{\partial x} - \frac{\partial V_1}{\partial y},$$

$$\frac{\partial U_2}{\partial t} + \nabla \cdot (U_2\mathbf{V}_2) = -\frac{\rho_1}{\rho_2} g_2 h_2 \frac{\partial h_1}{\partial x} - g_2 h_2 \frac{\partial h_2}{\partial x} + (f_0 + \beta_0 y)V_2 + A\Delta U_2 - R_2 U_2 + R_1(U_1 - U_2),$$

$$\frac{\partial V_2}{\partial t} + \nabla \cdot (V_2\mathbf{V}_2) = -\frac{\rho_1}{\rho_2} g_2 h_2 \frac{\partial h_1}{\partial y} - g_2 h_2 \frac{\partial h_2}{\partial y} - (f_0 + \beta_0 y)U_2 + A\Delta V_2 - R_2 V_2 + R_1(V_1 - V_2),$$

$$\frac{\partial h_2}{\partial t} = -\frac{\partial U_2}{\partial x} - \frac{\partial V_2}{\partial y}. \tag{1}$$

Here

$$U_i\mathbf{i} + V_i\mathbf{j} = h_i(u_i\mathbf{i} + v_i\mathbf{j}) = h_i\mathbf{V}_i, \qquad i = 1, 2,$$

are the two active-layer mass-flux vectors, where u_i, v_i represent the eastward and northward components of the upper- and lower-layer velocities, while h_1, h_2 are the upper- and lower-layer thicknesses. The two reduced gravities, $g_1 = g(\rho_3 - \rho_1)/\rho_3$ and $g_2 = g(\rho_3 - \rho_2)/\rho_3$, are assigned the values $g_1 = 4 \times 10^{-2}$ m s^{-2} and $g_2 = 8 \times 10^{-2}$ m s^{-2}, unless otherwise stated.

We represent horizontal eddy diffusion by an harmonic operator with a coefficient $A = 300$ m^2 s^{-1}. The bottom friction and the interface friction between the two active layers are both of Rayleigh type and are scaled by $R_1 = R_2 = 5 \times 10^{-8}$ s^{-1}. The value of the Rayleigh bottom-friction coefficient (R_2) corresponds to a typical decay (damping) timescale for the vorticity of 230 day^{-1} (see Stommel 1948; Pedlosky 1987; Jiang et al. 1995; Speich et al. 1995), although some authors use lower values of 60–120 day^{-1} (McCalpin and Haidvogel 1996; Primeau 1998). There is, however, no direct observational basis for choosing either value, since they correspond to a Stommel layer width of ≈6–12 km; this range of values is much smaller than the Munk boundary layer width δ_M (see section 5d below) that plays the more important role.

Standard midlatitude values for the Coriolis parameter's linearization are used in this study: $f_0 = 5 \times 10^{-5}$ s^{-1}, $\beta_0 = 2 \times 10^{-11}$ m^{-1} s^{-1}. Our upper ocean is driven by a steady, zonal wind stress with a sinusoidal profile

$$\tau^x(y) = -\tau_0 \cos(2\pi y/D) \tag{2}$$

that leads to the formation of a double gyre: an anticyclonic subtropical gyre and a cyclonic subpolar one (Verron and LeProvost 1978; Miller et al. 1987; Jiang et al. 1995).

No normal flow is allowed through the boundaries, and we use no-slip boundary conditions everywhere so that the system is consistent with the presence of the Laplace operator for $A \neq 0$. Some authors assume free-slip conditions (Chassignet and Gent 1991; Chang et al. 2001) or lateral boundary conditions that are intermediate between no slip and free slip (Jiang et al. 1995). Free-slip boundary conditions permit more energetic solutions, all other parameters being the same (see appendix *A* in Jiang et al. 1995). However, as pointed out by Meacham and Berloff (1997), this does not change the global stationary bifurcation structure of the system and stationary solutions have the same topological properties.

We write Eqs. (1) in nondimensional form by introducing the scalings

$$(u_i, v_i) = U(u_i', v_i'),$$

$$x = Lx', \qquad y = Ly', \qquad t = \frac{L}{U}t',$$

$$h_1 = H_1 h_1', \qquad h_2 = H_2 h_2', \qquad \tau = \tau_0 \tau'; \tag{3}$$

here $U = 1$ m s^{-1} is a typical velocity scale for western boundary currents, while $H_1 = H_2 = 500$ m correspond to the equilibrium depths of the two active layers. We note, however, that sensitivity experiments were also made using different values of H_2 (see section 5b). In most of the numerical simulations we choose $L = 1000$ km and $D = 2000$ km, respectively, but in section 2 of Part II much larger values of L and D will be considered as well.

With the scalings above, Eqs. (1) become

$$\frac{\partial U_1}{\partial t} + \nabla \cdot (U_1\mathbf{V}_1) = -F_1 h_1 \frac{\partial h_1}{\partial x} - F_2 h_1 \frac{\partial h_2}{\partial x} + (\epsilon^{-1} + \beta y)V_1 + \epsilon^{-1}E\Delta U_1 - \epsilon^{-1}\mu_1(U_1 - U_2) + \epsilon^{-1}\sigma\tau^x,$$

$$\frac{\partial V_1}{\partial t} + \nabla \cdot (V_1\mathbf{V}_1) = -F_1 h_1 \frac{\partial h_1}{\partial y} - F_2 h_1 \frac{\partial h_2}{\partial y} - (\epsilon^{-1} + \beta y)U_1 + \epsilon^{-1}E\Delta V_1 - \epsilon^{-1}\mu_1(V_1 - V_2),$$

$$\frac{\partial h_1}{\partial t} = -\frac{\partial U_1}{\partial x} - \frac{\partial V_1}{\partial y},$$

$$\frac{\partial U_2}{\partial t} + \nabla \cdot (U_2\mathbf{V}_2) = -\gamma F_1 h_2 \frac{\partial h_1}{\partial x} - F_2 h_2 \frac{\partial h_2}{\partial x} + (\epsilon^{-1} + \beta y)V_2 + \epsilon^{-1}E\Delta U_2 - \epsilon^{-1}\mu_2 U_2 + \epsilon^{-1}\mu_1(U_1 - U_2),$$

$$\frac{\partial V_2}{\partial t} + \nabla \cdot (V_2\mathbf{V}_2) = -\gamma F_1 h_2 \frac{\partial h_1}{\partial y} - F_2 h_2 \frac{\partial h_2}{\partial y} - (\epsilon^{-1} + \beta y)U_2 + \epsilon^{-1}E\Delta V_2 - \epsilon^{-1}\mu_2 V_2 + \epsilon^{-1}\mu_1(V_1 - V_2),$$

$$\frac{\partial h_2}{\partial t} = -\frac{\partial U_2}{\partial x} - \frac{\partial V_2}{\partial y}. \tag{4}$$

We supplement these nondimensional equations with the lateral no-slip boundary conditions:

$$U_i,\ V_i = 0 \quad \text{at } x = 0; \qquad L,\ y = 0,\ D. \tag{5}$$

The nondimensional parameters in Eqs. (4) are the Rossby number $\epsilon = U/(f_0 L)$, the inverse Froude numbers $F_1 = g_1 H_1/U^2$ and $F_2 = g_2 H_2/U^2$, the Ekman number $E = A/(f_0 L^2)$, the Rayleigh viscosity coefficients $\mu_1 = R_1/f_0$ and $\mu_2 = R_2/f_0$, the nondimensional wind-stress forcing $\sigma = \tau_0/(f_0 H_1 U \rho_1)$, the density ratio $\gamma = (\rho_1/\rho_2)(\rho_3 - \rho_2)/(\rho_3 - \rho_1)$, $0 < \gamma \leq 1$, and $\beta = \beta_0 L^2/U$. A more complete discussion of the nondimensional parameters in the double-gyre problem with vertical stratification is provided by Ghil et al. (2002b).

Conservation laws for Eqs. (4) can be obtained by integrating over the rectangular basin Ω and by making use of the no-slip conditions. They include mass conservation for each layer,

$$\int_\Omega (h_i - 1)\, d\omega = 0 \quad \text{for } i = 1, 2, \tag{6}$$

and total-energy conservation:

$$\frac{\partial(E_k + E_p)}{\partial t} = \mathcal{L} + \mathcal{R}_i + \mathcal{R}_b + \mathcal{W}, \tag{7}$$

with E_k being the kinetic energy, E_p the available potential energy, $\mathcal{L}$ the lateral friction, $\mathcal{R}_i$ the internal friction, $\mathcal{R}_b$ the bottom friction, and $\mathcal{W}$ the work exerted by the wind stress.

They are given by

$$E_k = \frac{1}{2}\int_\Omega (\gamma F_1 h_1 |\mathbf{V}_1|^2 + F_2 h_2 |\mathbf{V}_2|^2)\, d\omega,$$

$$E_p = \frac{1}{2}\int_\Omega \left[\gamma F_1^2 (h_1 - 1)^2 + F_2^2 (h_2 - 1)^2 + 2\gamma F_1 F_2 \frac{\rho_1}{\rho_2}(h_1 - 1)(h_2 - 1)\right] d\omega,$$

$$\mathcal{L} = \epsilon^{-1} E \int_\Omega [\gamma F_1 \mathbf{V}_1 \cdot \Delta(h_1 \mathbf{V}_1) + F_2 \mathbf{V}_2 \cdot \Delta(h_2 \mathbf{V}_2)]\, d\omega,$$

$$\mathcal{R}_i = -\epsilon^{-1}\mu_1 \int_\Omega [(U_1 - U_2)(\gamma F_1 u_1 - F_2 u_2) + (V_1 - V_2)(\gamma F_1 v_1 - F_2 v_2)]\, d\omega,$$

$$\mathcal{R}_b = -\epsilon^{-1}\mu_2 F_2 \int_\Omega |\mathbf{V}_2|^2 h_2\, d\omega,$$

$$\mathcal{W} = \gamma F_1 \int_\Omega \mathbf{V}_1 \cdot \boldsymbol{\tau}\, d\omega. \tag{8}$$

Note that when $\rho_1 = \rho_2$, so that $\gamma = 1$, the velocities are continuous at the interface and the interface friction reduces to zero. The internal friction $\mathcal{R}_i$ is negative definite provided $u_2 \ll u_1$ and $v_2 \ll v_1$; this is always the case within a reasonably realistic parameter range and has been verified for all our numerical simulations. Its role is thus similar to the bottom friction term and they both act as dissipation mechanisms.

b. Quasigeostrophy in the SW equations

To compare our results with those of 2½-layer QG models, we summarize here the QG equations related to our 2½-layer SW model, using a standard scaling argument. The smallness of the Rossby number ϵ induces a dominant geostrophic balance between Coriolis and pressure forces. Let us write the two layers' thicknesses as

$$h_i = H_i + K_i \eta_i, \quad i = 1, 2. \tag{9}$$

Substituting (9) in (4) and choosing K_i such that the desired dynamical balance is achieved gives

$$\epsilon\left(\frac{\partial u_i}{\partial t} + \mathbf{V}_i \cdot \nabla u_i\right) = -\gamma_i \frac{\partial \eta_1}{\partial x} - \frac{\partial \eta_2}{\partial x} + (1 + \epsilon\beta y) v_i + E\Delta u_i + \delta_{i1}\sigma\tau^x,$$

$$\epsilon\left(\frac{\partial v_i}{\partial t} + \mathbf{V}_i \cdot \nabla v_i\right) = -\gamma_i \frac{\partial \eta_1}{\partial y} - \frac{\partial \eta_2}{\partial y} - (1 + \epsilon\beta y) u_i + E\Delta v_i,$$

$$\epsilon\left(\frac{\partial \eta_i}{\partial t} + \mathbf{V}_i \cdot \nabla \eta_i\right) = -\frac{\lambda_i^2}{H_i} h_i \nabla \cdot \mathbf{V}_i; \tag{10}$$

here $\lambda_i^{-2} = (L/L_{R,i})^2$ are the nondimensional Rossby deformation radii, with $L_{R,i} = (g_i H_i)^{1/2}/f_0$, $\gamma_1 = 1$, $\gamma_2 = \gamma$, and δ_{i1} is the Kronecker symbol. For simplicity, we have omitted the interface friction terms. The upper- and lower-layer thicknesses become

$$h_i = H_i(1 + \epsilon\lambda_i^{-2}\eta_i). \tag{11}$$

For small ϵ, we expand the variables η_i, u_i, v_i in an asymptotic series in ϵ, for instance $\eta_i = \eta_i^0 + \epsilon\eta_i^1 + O(\epsilon^2)$. The expansion of Eq. (10) to the zero*th* order gives the geostrophic equilibrium,

$$\nabla\Psi_i = \mathbf{k} \times \mathbf{V}_i^0, \tag{12}$$

where $\Psi_i = \gamma_i \eta_1^0 + \eta_2^0$ are the streamfunctions of the two active layers. The first-order approximation of (10) yields the nondimensional potential-vorticity equations,

$$\frac{\partial \xi_1}{\partial t} + J(\Psi_1, \xi_1) + \beta\frac{\partial \Psi_1}{\partial x} = E\nabla^4\Psi_1 + \sigma\nabla \times \tau,$$

$$\frac{\partial \xi_2}{\partial t} + J(\Psi_2, \xi_2) + \beta\frac{\partial \Psi_2}{\partial x} = E\nabla^4\Psi_2. \tag{13}$$

The potential vorticities of the lower and upper layers are connected with the streamfunctions through the coupled elliptic equations

$$\Delta\Psi_1 - \frac{\lambda_1^{-2}}{1-\gamma}(\Psi_1 - \Psi_2) = \xi_1,$$
$$\Delta\Psi_2 - \frac{\lambda_2^{-2}}{1-\gamma}(\Psi_2 - \gamma\Psi_1) = \xi_2. \quad (14)$$

The barotropic and baroclinic components are, respectively,

$$\Psi_1 + \Psi_2 = \epsilon\left[\frac{(1+\gamma)}{2}F_1h_1 + F_2h_2\right],$$
$$\Psi_1 - \Psi_2 = \epsilon\frac{(1-\gamma)}{2}F_1h_1. \quad (15)$$

Plotting the QG streamfunctions Ψ_i and the eigenvectors ψ_i, which destabilize them, enables us to better visualize baroclinic modes. The total streamfunction fields Ψ_i are expressed in terms of the layer-thickness deviations η_i using (11) and the expressions of the inverse Froude numbers,

$$\Psi_1 = \eta_1 + \eta_2 = \epsilon(F_1h_1 + F_2h_2),$$
$$\Psi_2 = \gamma\eta_1 + \eta_2 = \epsilon(\gamma F_1h_1 + F_2h_2). \quad (16)$$

The eigenmodes ψ_i associated with Ψ_i are likewise equal to $\epsilon(\gamma_i F_1 h_1' + F_2 h_2')$; here h_i' are the upper- and lower-layer thickness eigenvectors obtained from the linear stability analysis of a steady-state solution of Eq. (4), while $\gamma_1 = 1$ and $\gamma_2 = \gamma$.

3. Numerical methods

Equations (4), when discretized in space, can be written in the form of a system of nonlinear coupled ordinary differential equations (ODEs):

$$\dot{\mathbf{W}} = \mathbf{F}(\mathbf{W}; \mathbf{P}). \quad (17)$$

Here $\mathbf{W} = (U_1, V_1, h_1, U_2, V_2, h_2)$ is the state-variable vector, $\dot{\mathbf{W}} = d\mathbf{W}/dt$, $\mathbf{F} = (f_1, f_2, f_3, f_4, f_5, f_6)$ is the corresponding discretized right-hand side, and $\mathbf{P} = (\epsilon, F_1, F_2, E, \mu_1, \mu_2, \beta, \sigma)$ is the parameter vector.

Ghil et al. (2002b) provide a complete discussion of the total number of independent parameters for a two-mode QG model of the wind-driven circulation. These authors also review briefly previous studies of the double-gyre circulation in terms of the subset of parameters that were varied systematically to help understand the circulation's low-frequency variability. For the present 2½-layer SW model, the number of independent parameters is 8, one larger than in rigid-lid QG models with two layers or two modes. The main parameters that will be varied are the intensity σ of the wind stress and the lower layer's inverse Froude number F_2. Robustness of the solutions' bifurcation structure will also be studied with respect to the interface Rayleigh viscosity μ_1, the spatial resolution, and the asymmetry of the wind stress pattern.

Space differencing is performed on a standard Arakawa C-grid (Arakawa and Lamb 1977). For the nonlinear advection term, a variant of the Lilly scheme (Scheme C in Grammeltvedt 1969) is adopted. This scheme conserves the system's total energy in the absence of friction.

Our aim is to compute the branching structure of Eqs. (4). A first step is to start from a stationary solution. We solve thus

$$\mathbf{F}(\mathbf{W}; \mathbf{P}) = 0, \quad (18)$$

and compute a branch of solutions as one specific parameter in $\mathbf{P}$ varies. This is achieved by using Keller's (1977) pseudo-arclength continuation method. One advantage of pseudo-arclength methods is the possibility of computing unstable steady-state solutions and of showing how branches of stable solutions are connected. Continuation methods have already been used in atmospheric models of intermediate resolution (Legras and Ghil 1985), as well as in higher-resolution ocean models (Speich et al. 1995). We refer to Kubiček and Marek (1983) and Seydel (1994) for further details on the use of pseudo-arclength methods in the numerical study of bifurcation problems.

Furthermore, we investigate the linear stability of each solution on a given branch. This involves computing the Jacobian matrix $\mathbf{J} = \partial\mathbf{F}/\partial\mathbf{W}$. Because of the ill-conditioned nature of the matrix $\mathbf{J}$, we need direct solvers for the implied inverse of $\mathbf{J}$. To exploit the sparse structure of $\mathbf{J}$, we carry out its $\mathbf{LU}$ decomposition by applying the unsymmetric-pattern multifrontal method of Davis and Duff (1997). Using such direct solvers, rather than iterative ones, may however seriously restrict the number of unknowns.

In the present study, the size of the domain has been dictated by the compromise between a marginally eddy-resolving grid of $\Delta x = \Delta y = 20$ km and the total number n of discrete variables. To use the numerical continuation method we have to solve two $n \times n$ linear systems at each Newton iteration step of the method. Our numerical methods allow us to use $n = 30\,000$, namely 5000 grid points for the six unknowns, which yields a domain size of $L \times D = 1000 \times 2000$ km for our rectangular basin.

To compute the linear stability of the solutions at each step of the continuation method, we write (17) in the more general form

$$\mathbf{G}(\mathbf{W}, \dot{\mathbf{W}}; \mathbf{P}) = \mathbf{0}. \quad (19)$$

This is the form that the QG system's spatially discretized version usually takes. The appearance of the time derivatives $\dot{\mathbf{W}}$ in this implicit form is due to the presence of the time-independent boundary conditions. For small disturbances $\boldsymbol{\delta}$ imposed on a steady state $\mathbf{W}_0$, the linearized version of (19) reads

$$\mathbf{G}_{\dot{\mathbf{W}}}(\mathbf{W}_0, \mathbf{0}; \mathbf{P})\frac{\partial\boldsymbol{\delta}}{\partial t} + \mathbf{G}_{\mathbf{W}}(\mathbf{W}_0, \mathbf{0}; \mathbf{P})\boldsymbol{\delta} = \mathbf{0}. \quad (20)$$

To solve the system of ODEs (20) mode by mode,

we consider the generalized eigenvectors $\boldsymbol{\varphi}_i$ that solve the generalized eigenvalue problem,

$$\mathbf{A}\boldsymbol{\varphi} = \eta\mathbf{B}\boldsymbol{\varphi} \tag{21}$$

with $\mathbf{A} = \mathbf{G}_w(\mathbf{W}_0, \mathbf{0}; \mathbf{P})$ and $\mathbf{B} = -\mathbf{G}_{\dot{w}}(\mathbf{W}_0, \mathbf{0}; \mathbf{P})$. In a finite-difference discretization, $\mathbf{B}$ is diagonal and may be singular because of the boundary conditions (5). A steady-state flow is linearly stable when all eigenvalues have strictly negative real parts. As one of the parameters varies, the stability of the steady state $\mathbf{W}_0$ changes when the leading eigenvalue η crosses the imaginary axis. The manifold of this parameter's critical values, for which $\mathrm{Re}(\eta) = 0$, marks the boundary between stable and unstable solutions. If $\mathrm{Im}(\eta_0) \neq 0$, then a Hopf bifurcation occurs at the critical value η_0 and there is no change of sign of the determinant of the Jacobian $\mathbf{J}$ when crossing the neutral-stability manifold $\mathrm{Re}(\eta) = 0$ at $\eta = \eta_0$.

For problems of this size, $n = O(10^4)$, it is impossible to use traditional eigenvalue solvers that determine all the eigenvalues and, if desired, all the eigenvectors. However in many hydrodynamic stability problems, the initial instability of a certain steady flow pattern occurs only through a few modes. In the discretized linear stability problem (21), one wishes, therefore, to compute a small number of eigenmodes, that is, those with eigenvalues closest to the imaginary axis; these eigenmodes are often referred to as the ''dangerous'' ones. To do so, we follow Speich et al. (1995) and use a combination of the spectral transform (Christodoulou and Scriven 1988) and the simultaneous iteration algorithm (Stewart and Jennings 1981).

The idea of this algorithm is to transform the eigenvalue problem in such a way that the most dangerous modes become dominant, as they become associated with the largest absolute values. The spectral transform used here is a complex mapping applied to the generalized eigenvalue η,

$$\eta = b + a\frac{\kappa - 1}{\kappa + 1}, \tag{22}$$

where b is real and a is positive. The parameter b shifts the generalized spectrum along the real axis, whereas the parameter a stretches it. The left complex plane $\mathrm{Re}(\eta - b) < 0$ is mapped onto the unit disk $|k| < 1$, and the imaginary axis $\mathrm{Re}(\eta - b) = 0$ is mapped onto the unit circle $|k| = 1$.

The eigenvalue problem (21) is transformed by (22) into

$$\mathbf{C}\mathbf{x} = \mathbf{D}k\mathbf{x}, \tag{23}$$

where $\mathbf{C} = \mathbf{A} + (a - b)\mathbf{B}$, $\mathbf{D} = -\mathbf{A} + (a + b)\mathbf{B}$ and $\mathbf{x}$ is a generalized eigenvector of (23). Although $\mathbf{B}$ is singular, the matrices $\mathbf{C}$ and $\mathbf{D}$ are generically nonsingular and we therefore consider the problem

$$\mathbf{E}\mathbf{x} = \mathbf{D}^{-1}\mathbf{C}\mathbf{x} = \kappa\mathbf{x}. \tag{24}$$

In this way, generalized power methods (Golub and Van Loan 1996) can be used on the transformed problem. In the process of applying such a method to Eq. (24), we use the **LU** decomposition of Davis and Duff (1997) on $\mathbf{D}$ as well.

Equations (17) are a discretized form of the forced-dissipative PDE system (4). We expect that the solution trajectories—starting from any given initial state in their finite-dimensional phase space—converge to an attractor with much lower dimension than n. This could be either a limit cycle, that is, a periodic solution of (17), a torus (quasi periodic), or a chaotic (fractal) attractor (e.g., Ghil and Childress 1987; Temam 1998). In order to classify such finite-dimensional attractors we need to integrate the ODEs (17) over a long time interval T_0; we use $T_0 \geq 150$ yr in most of our simulations, for which we adopted a space-centered Euler backward (Matsuno) scheme. Domain decomposition was used in order to save computer time since the time step Δt is less than 20 min in most of the simulations.

At each time step we compute kinetic and potential energy and other diagnostic quantities that characterize the flow pattern. We then subject the time series of these global state variables to singular-spectrum analysis (SSA) in order to extract the system's principal modes of low-frequency variability. SSA is by now a well-established advanced method for the spectral analysis of oceanographic (Colebrook 1978), as well as nonlinear (Broomhead and King 1986), atmospheric (Fraedrich 1986), and climatic (Vautard and Ghil 1989) time series. We refer to Dettinger et al. (1995) and Ghil et al. (2002a) for the methodology and its applications.

4. Bifurcation structure

a. General approach

We now explore different regimes of the 2½-layer SW model as the parameters vary. We first compute the bifurcation diagrams of the steady-state solutions. The control parameter under consideration is always plotted on the abscissa. The quantity that characterizes the solution on the ordinate is chosen, following Chang et al. (2001), to be the normalized transport difference TD. We define it here as

$$\mathrm{TD} = \frac{(h_{1,\mathrm{MAX}} + h_{1,\mathrm{MIN}} - 2)}{\max\{|h_{1,\mathrm{MAX}} - 1|, |h_{1,\mathrm{MIN}} - 1|\}}, \tag{25}$$

where $h_{1,\mathrm{MAX}}$ is the maximum and $h_{1,\mathrm{MIN}}$ is the minimum of h_1 over the rectangular domain Ω. The strength of the subtropical gyre is proportional to the quantity $h_{1,\mathrm{MAX}} - 1$ and that of the subpolar gyre to $h_{1,\mathrm{MIN}} - 1$.

Zero transport difference between the gyres, TD = 0, corresponds to a perfectly (anti-) symmetric solution, with two counterrotating gyres of equal strength and spatial extent. A negative TD value corresponds, as we shall see, to a solution with a subpolar, cyclonic gyre that is more intense than the subtropical, anticyclonic gyre but smaller in spatial extent than the latter; these

TABLE 1. Reference values of the model's nondimensional parameters.

Parameter	σ	ϵ	β	E	μ_1	μ_2	F_1	F_2
Value	2.5×10^{-3}	0.02	20	0.6×10^{-5}	10^{-3}	10^{-3}	20	4.0

solutions will be called ''subpolar.'' Conversely, TD $>$ 0 corresponds to a subtropical gyre that has a smaller extent but is stronger than the subpolar one; we call these solutions ''subtropical.'' Note that the definition of TD used by Chang et al. (2001)—based on the streamfunction values in their model's barotropic vorticity equation—results in associating TD $\gtrless 0$ with the same branches of the bifurcation diagram as ours. In our SW model, however, we do not expect a perfectly symmetric steady state with TD $= 0$ for small σ, like in Chang et al.'s model (see below).

In the following bifurcation diagrams, solid lines indicate stable branches and dashed lines unstable ones. The singularities of the bifurcation curves are labeled with L for limit or turning points, that is, saddle-node bifurcations, and with HB for Hopf bifurcation points. The flow patterns associated with the bifurcation diagrams are contour plots of the upper- and lower-layer streamfunctions, together with their maxima, minima, and contour interval in nondimensional units. For both the steady-state and the time-evolving computations, the numerical methods we use impose mass conservation (6) in each layer; that is, the mean value of the h_1 and h_2 deviations must be zero.

The reference values of the dimensionless parameters are given in Table 1. In each bifurcation diagram hereafter, one of these parameters varies, while the others are kept constant at the values shown in the table.

b. Dependence on wind stress forcing

The bifurcation diagram of steady-state solutions, for varying amplitudes σ of the wind stress, is shown in Fig. 2. The subpolar branch is continuous across the entire range of σ values examined, starting at $\sigma = 0$. It is, therefore, easy to obtain in a straightforward manner by starting from a solution at rest, with zero velocities and $h_1 \equiv h_2 \equiv 1$, and using the continuation method with respect to the parameter σ.

The isolated branch of steady solutions in Fig. 2 is made up of the perturbed-symmetric and the subtropical branch, both of which start at $\sigma > 2 \times 10^{-3}$ and do not connect to the subpolar one. It is thus quite difficult to compute this branch if one does not take into account the inherent mathematical structure of the problem at hand. To wit, the branching structure of the QG equations is of pitchfork type (Cessi and Ierley 1995; Jiang et al. 1995), with connected branches due to reflection symmetry through the mid axis ($y = D/2$) of the basin since the PDEs, boundary conditions and forcing all admit this symmetry. This is topologically different from the SW models (Jiang et al. 1995; Speich et al. 1995; Dijkstra and Molemaker 1999), where the symmetry-breaking bifurcation is of perturbed pitchfork type; that is, the three connected branches of the perfect pitchfork bifurcation become disconnected.

We know, however, that the isolated, subtropical + symmetric branch of solutions in the latter case is a perturbation of the corresponding two branches in the former. We computed therefore the subtropical + symmetric branch in the following way. In the absence of interfacial and bottom friction; that is, when $\mu_1 = \mu_2 = 0$, there exists a trivial solution of our 2½-layer model (4). This solution has a motionless second layer $U_2 = V_2 = 0$, $h_2 = -\gamma(F_1/F_2)h_1$, while the motion in the upper layer (U_1, V_1, h_1) is a solution of the 1½-layer SW equations with $F = (1 - \gamma)F_1$. A subtropical-branch solution for this 1½-layer model is easily obtained using reflection symmetry. Indeed, for well-chosen values of σ, the flow pattern that is symmetric with respect to the subpolar-branch solution usually belongs to the basin of attraction of the subtropical-branch solution that we are looking for. This solution is then found by using the Newton method.

Next, we return to the 2½-layer model by continuation in μ_1 and μ_2 until we reach the right values of the parameters. We are thus able to connect smoothly the 2½-layer model (4) to the 1½-layer model. In essentially the same way as Speich et al. (1995) obtained a perturbed pitchfork bifurcation for the latter, we thus obtain it for our 2½-layer model. However, we will describe in section 4d a simpler and more systematic way to find the isolated branch.

For small wind-stress amplitude $\sigma \leq 1.5 \times 10^{-3}$, we obtain a unique steady-state solution that belongs to the subpolar branch. We note that the graphic representation of the subtropical and subpolar branch as either the upper or the lower branch in a bifurcation diagram depends on the scalar quantity chosen to represent the solution on the ordinate of the bifurcation diagram. The ''ordering'' of the branches here is the same as in Speich et al. (1995) and Chang et al. (2001). It is opposite to that of Jiang et al. (1995), who used the latitudinal position of the merger point between the two boundary currents—after separation from the western boundary, as they form the model's eastward jet—to plot on their ordinate.

The flow pattern on the low-wind-stress portion of the branch (not shown) is close to (anti-)symmetric, while the transport difference is negative. In our SW model, the slope of the sea surface and of the thermocline associated with the eastward jet on a β plane break the symmetry. This is reflected by the fact that the transport difference TD for the subpolar branch is not zero when the wind stress intensity σ is small (see also Dijkstra and Molemaker 1999), while in a QG model TD must be zero in this case (Chang et al. 2001). The second layer is almost motionless and deviations

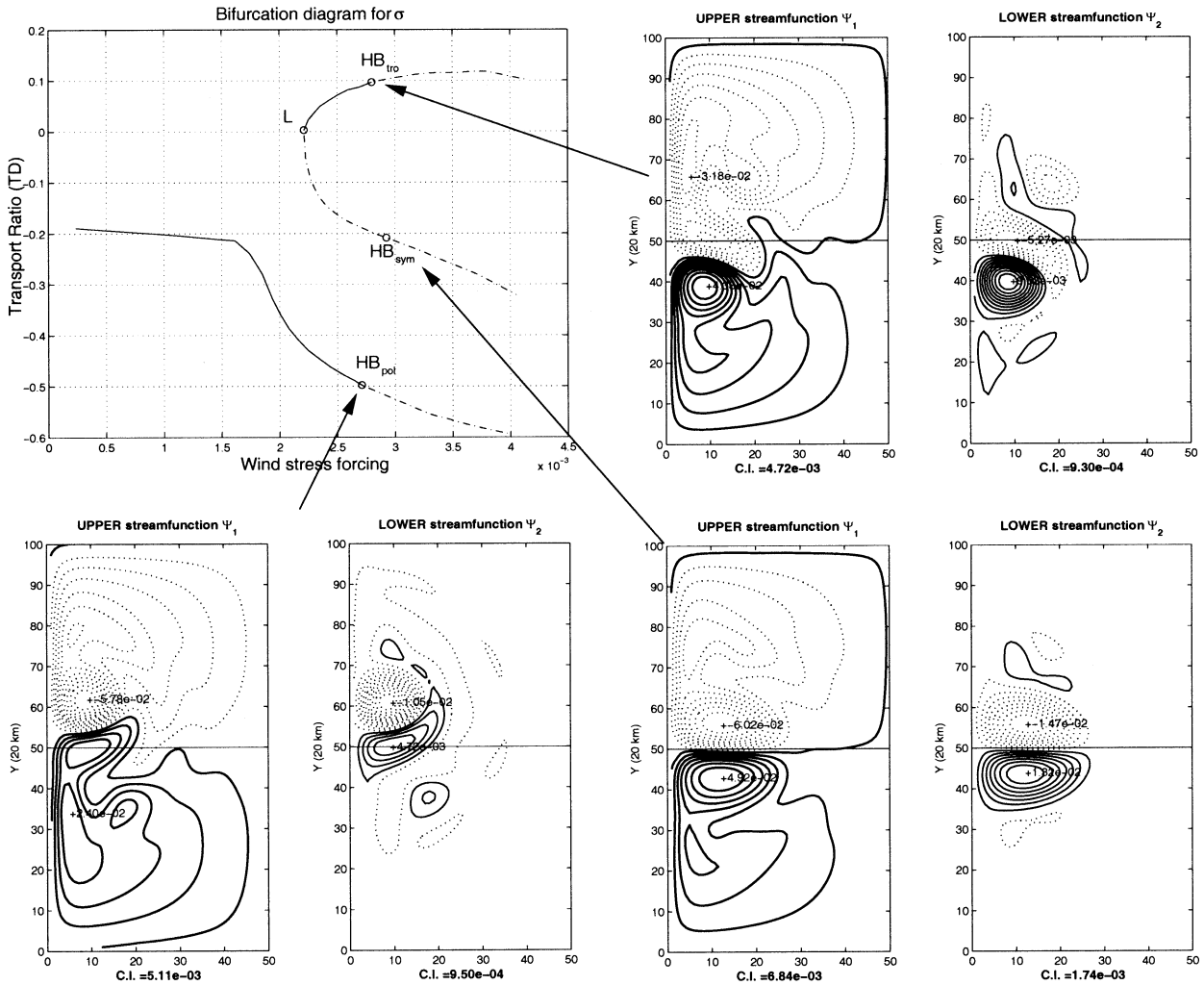

FIG. 2. Bifurcation diagram with respect to the wind stress intensity σ; the normalized transport difference TD is plotted vs σ. The streamfunction flow patterns at Hopf bifurcation are referred by arrows to the appropriate location on the subpolar branch, $\sigma_{\mathrm{HB}}^{(\mathrm{pol})} = 2.717 \times 10^{-3}$; perturbed symmetric branch, $\sigma_{\mathrm{HB}}^{(\mathrm{sym})} = 2.901 \times 10^{-3}$; and subtropical branch, $\sigma_{\mathrm{HB}}^{(\mathrm{tro})} = 2.821 \times 10^{-3}$.

of its thickness from a constant are similar to the upper layer with the sign reversed (not shown either).

We have confirmed, by looking at very small values of σ, that TD $\neq 0$ for $\sigma \to 0$. The slight difference between the subpolar and subtropical thickness deviations yields a nonzero value of TD $= -0.2$ in the limit of zero wind stress intensity. More precisely, the subtropical limit is $h_{1,\mathrm{MAX}} = 1 + K^{\mathrm{tro}}\sigma + O(\sigma^2)$ and the subpolar one is $h_{1,\mathrm{MIN}} = 1 - K^{\mathrm{pol}}\sigma + O(\sigma^2)$; hence the quantity TD converges to $(K^{\mathrm{tro}} - K^{\mathrm{pol}})/\max(K^{\mathrm{pol}}, K^{\mathrm{tro}})$. In the SW case $K^{\mathrm{tro}} \neq K^{\mathrm{pol}}$, whereas in the symmetric QG case $K^{\mathrm{tro}} = K^{\mathrm{pol}}$. Although the limit $\sigma \to 0$ yields a system of linear PDEs, it is not known in general how K^{tro} and K^{pol} depend on the geometry and the physical parameters of the problem. In the present case it appears that $K^{\mathrm{tro}} < K^{\mathrm{pol}}$, so the subpolar branch is chosen first. This point is also discussed in section 5d.

For σ larger than 1.6×10^{-3}, the transport difference decreases suddenly as the subpolar gyre's intensity increases. The flow patterns become more and more asymmetric, like the one shown at the bottom of Fig. 2. In the upper layer, the greater strength of the subpolar gyre is associated with the formation of an intense recirculation vortex near its western boundary and the symmetry axis. A weaker vortex of opposite polarity is formed in the corresponding position within the subtropical gyre. We shall refer to these inertial recirculation features as cells or vortices to distinguish them from the basinwide gyres that are dominated by Sverdrup balance (see also Ghil et al. 2002b).

The subtropical gyre's greater spatial extent results from the poleward overshooting of its western boundary current and the formation of the eastward jet on the poleward side of the domain's symmetry axis. The

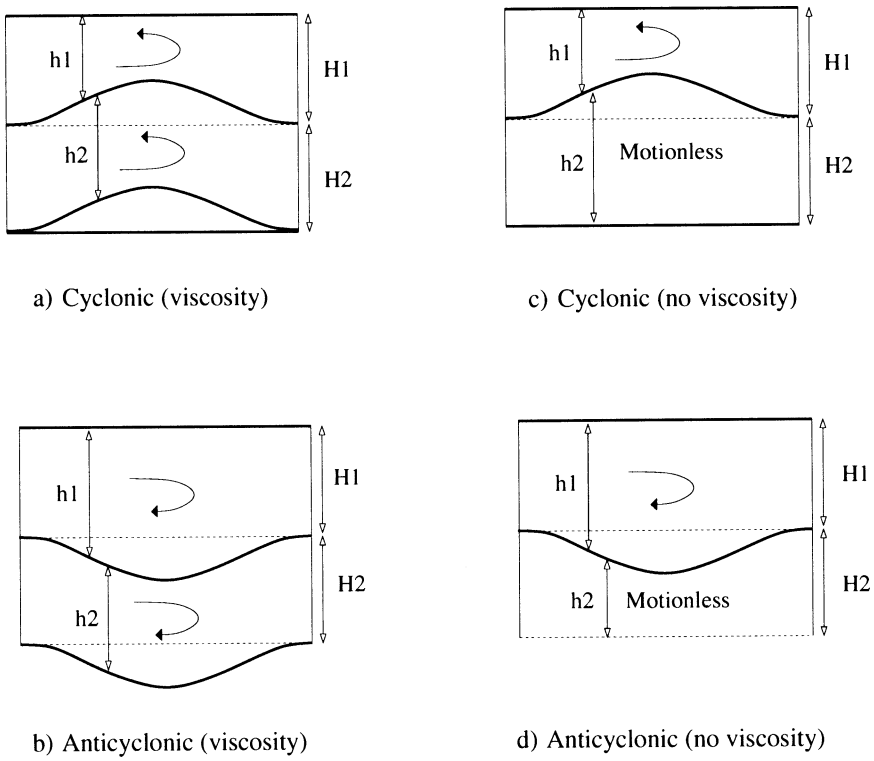

FIG. 3. Schematic diagram of the flow in the two layers: for a strong (a), (c) cyclonic and (b), (d) anticyclonic circulation. Here (a) and (b) represent flow with interfacial friction, $\mu_1 \neq 0$; for (c) and (d), $\mu_1 = 0$.

abrupt change of TD past $\sigma = 1.6 \times 10^{-3}$ is, in fact, related to a change in the position of the minimum upper-layer thickness, which lies just off the southward-flowing western boundary current when $\sigma < 1.6 \times 10^{-3}$, while it lies farther offshore, just poleward of the subpolar recirculation cell, when $\sigma > 1.6 \times 10^{-3}$. Global quantities, however, like the kinetic and potential energy, evolve smoothly as σ increases (not shown).

As the cyclonic recirculation cell gains in intensity, the second layer is sucked up, while keeping a thickness that is approximately constant, $h_2 \simeq 1$, but still larger than its thickness at rest, $h_2 \geq 1$ (see Fig. 3a). Likewise, the second layer keeps its thickness approximately constant as it is being pushed down under the anticyclonic recirculation cell (see Fig. 3b). Figures 3a and 3b show schematically that the thickness deviations in the second layer, while small, are in general of opposite sign to those found in the upper layer. A comparison of Figs. 3c and 3d (where interface friction is zero) with Figs. 3a and 3b (where it is not) indicates that the interaction between the two layers through the interface friction term is fairly substantial in the inertial recirculation region.

The velocity fields in both active layers (not shown) are more intense overall in the stronger subpolar recirculation cell. They are weaker in the second layer, due to the negative interference between the flow's baroclinic component, which changes sign between the two active layers, and the barotropic component, which does not (see Ghil et al. 2002b).

For σ greater than 2.21×10^{-3}, we obtain a subtropical and a perturbed-symmetric branch, one stable and the other one unstable; neither is connected to the subpolar branch at any parameter values that we have explored. Near the limit point L at the merger of these two branches, two counterrotating vortices appear on the unstable symmetric branch in the inertial recirculation zone; they gain in intensity in both layers as σ increases (middle-right panel in Fig. 2). The solutions on this branch are nearly antisymmetric, with an only slightly stronger subpolar cell. They resemble therein the solutions on the subpolar branch at low σ (not shown) but are more intense and hence unstable (see also Speich et al. 1995).

As we increase the forcing parameter along the subtropical stable branch (upper-right panel in Fig. 2), the subtropical cell is stronger and tighter in spatial extent, as expected from earlier work. The strong anticyclonic recirculation vortex in the upper layer is accompanied by a smaller and weaker vortex of the same sign in the lower layer, indicating the predominance of barotropic flow in the inertial recirculation zone (see Ghil et al. 2002b).

The first branch to lose its stability is the subpolar branch; we obtain a Hopf bifurcation for $\sigma_{\mathrm{HB}}^{(\mathrm{pol})} = 2.717 \times 10^{-3}$ with a subannual period of $T = 148$ days. This agrees quite well with the Hopf bifurcation off the two

symmetric branches in Chang et al.'s (2001) QG barotropic model. The next Hopf bifurcation is off the stable subtropical branch at $\sigma_{\mathrm{HB}}^{(\mathrm{tro})} = 2.821 \times 10^{-3}$ and has an interannual period of $T = 704$ days. This result is slightly different from the one found in Speich et al. (1995), as the subtropical branch lost its stability more easily through primary Hopf bifurcation for the region of parameter space they explored. We will see in section 3 of Part II, however, that the time-dependent solutions off the subtropical branch are not very stable and contribute only indirectly to the low-frequency variability that prevails in the aperiodic regime.

The first oscillatory mode that arises of the subpolar branch has thus a much higher frequency than the one off the subtropical branch: the period associated with the unstable mode for the latter is almost five times longer than for the subpolar branch. This was already observed in the 1½-layer SW model of Jiang et al. (1995) and Speich et al. (1995). We will investigate in greater detail this phenomenon in section 2 of Part II. Finally, the unstable symmetric branch also undergoes a Hopf bifurcation, and an unstable limit cycle develops for $\sigma_{\mathrm{HB}}^{(\mathrm{sym})} = 2.901 \times 10^{-3}$, with a period of $T = 243$ days.

For a QG barotropic model with large aspect ratio L_x/L_y (Primeau 1998), a larger number of stationary solution branches arises for higher values of σ. These are due to the appearance, via additional pitchfork bifurcations, of further stationary-solution branches that are associated with additional meanders along the eastward jet. Ghil et al. (2002b) provide some analytical support for Primeau's numerical evidence, still in a QG framework. Many QG studies, however, exhibit three distinct connected branches (Cessi and Ierley 1995; Dijkstra and Katsman 1997), one symmetric and the other two asymmetric, with different qualitative features; the latter arise from two successive pitchfork bifurcations. This QG picture stands in contrast with the SW case, in which only two connected branches, both related to the first, perturbed pitchfork bifurcation have ever been found.

5. Sensitivity results

In this section, we compute bifurcation diagrams like those in Fig. 2 with respect to additional parameters: the Rayleigh viscosity parameter μ_1, the inverse Froude number F_2 of the lower active layer, and the asymmetry s of the wind stress forcing (to be defined in section 5c below). In each case, all other parameters have the value given in Table 1. We also consider the dependence of the critical values for saddle node and Hopf bifurcation with respect to one parameter, such as wind stress intensity σ, on the values of another parameter, such as F_2. Last, the robustness of our bifurcation results to the model's spatial resolution is investigated.

a. Dependence on the interface friction

We let the Rayleigh viscosity parameter μ_1 vary first. It acts as a dissipation parameter, and we expect it therefore to lead to less complex flows as it increases. Moreover, μ_1 gives also the strength of the interaction between the two active layers: for $\mu_1 = 0$ the two layers are essentially uncoupled and the solution of Eqs. (4) is the 1½-layer solution described at the beginning of section 4b. We use $1/\mu_1$ as the abscissa in Fig. 4 in order to obtain incease of complexity along the abscissa, as in Fig. 2. For a value of μ_1 greater than 1.8×10^{-3} (i.e., $1/\mu_1 \leq 5.5 \times 10^2$) we obtain only one branch of stationary solutions, to wit, the subpolar branch.

For small values of $1/\mu_1$ (lower-left panel in Fig. 4), the two gyres are relatively weak and nearly antisymmetric. In the bifurcation diagram, we observe a sharp change in the slope of the transport difference TD versus $1/\mu_1$ at about $1/\mu_1 \simeq 4 \times 10^2$. The value of TD for smaller $1/\mu_1$ (i.e., for $\mu_1 \geq 2.5 \times 10^{-3}$) is nearly constant and approximately equal to -0.2. This is precisely the value we obtained for small wind-stress intensity in Fig. 2.

As we increase $1/\mu_1$ further, we obtain the two additional branches, perturbed-symmetric and subtropical. The flow patterns on the two stable branches, subpolar (lower branch in Fig. 4) and subtropical (upper branch in Fig. 4), look very similar to the corresponding solutions obtained by varying σ (Fig. 2). The flow on the unstable symmetric branch (upper-right panel in Fig. 4), exhibits an almost symmetric dipole in the inertial recirculation zone; this dipole is more elongated in the E–W direction than is the case for the stable branches (see also Fig. 2).

As $1/\mu_1$ increases, we obtain nearly the same spatial patterns for h_1 and h_2 (not shown), only with the signs reversed, since the lower layer interacts less with the top layer. This behavior is the same as the one obtained by Dijkstra and Katsman (1997) in their two-layer QG model: since they neglected interface friction, their lower layer interacted only through the pressure term with the upper layer.

All three steady-state branches are again destabilized by Hopf bifurcation. The subpolar branch is destabilized first for $\mu_{\mathrm{HB}}^{(\mathrm{pol})} = 0.6824 \times 10^{-3}$ with a period $T = 127$ days, then the subtropical branch for $\mu_{\mathrm{HB}}^{(\mathrm{tro})} = 0.6756 \times 10^{-3}$ with $T = 140$ days, and finally the unstable branch gives rise to an unstable limit cycle for $\mu_{\mathrm{HB}}^{(\mathrm{sym})} = 0.2747 \times 10^{-3}$ and $T = 248$ days. The periods associated with the oscillatory instabilities off the perturbed-symmetric and the subpolar branch here are quite close to those obtained by increasing the wind stress σ in Fig. 2 (243 vs 248 days and 148 vs 127 days).

b. Dependence on inverse Froude number

We recall that $F_2 = g[(\rho_3 - \rho_2)/\rho_3]H_2/U^2$ is the lower-layer inverse Froude number. Letting this parameter vary may be interpreted either as a change of the lower-layer reference thickness H_2 or as a change in the internal deformation radius $L_{R,2} = (g_2 H_2)^{1/2}/f_0$ (see sec-

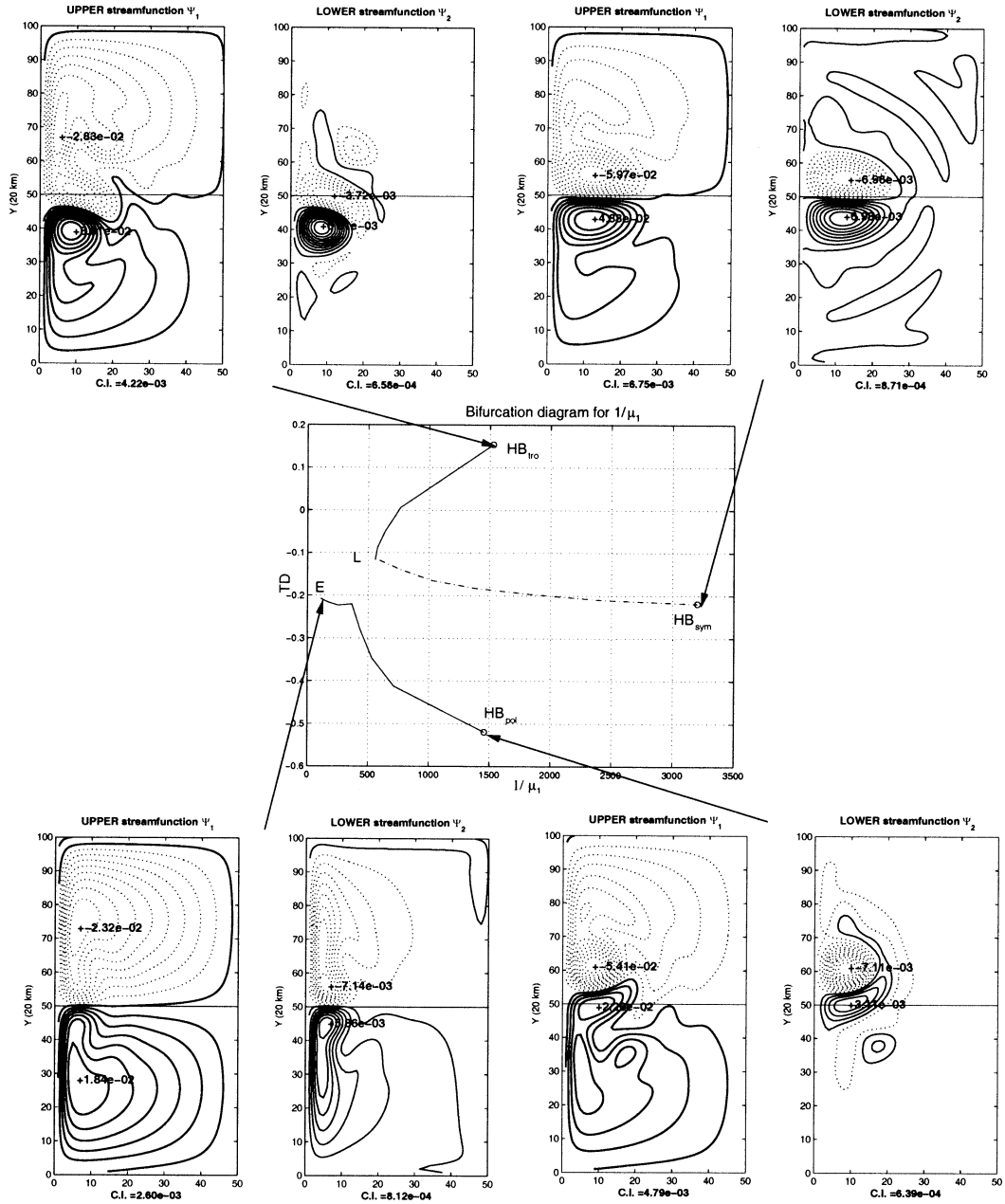

FIG. 4. Bifurcation diagram for the Rayleigh viscosity parameter μ_1; in the central panel TD is plotted vs $1/\mu_1$. The flow patterns are referred by arrows to points in the central panel, as in Fig. 2: (lower-left) the steady state at $\mu_1 = 10^{-2}$; (lower right) the Hopf bifurcation on the subpolar branch, $\mu_{\mathrm{HB}}^{(\mathrm{pol})} = 0.6824 \times 10^{-3}$; (upper right) the perturbed symmetric branch, $\mu_{\mathrm{HB}}^{(\mathrm{sym})} = 0.2747 \times 10^{-3}$; and (upper left) the subtropical branch, $\mu_{\mathrm{HB}}^{(\mathrm{tro})} = 0.6756 \times 10^{-3}$.

tion 2b) or both. By doing so, we obtain a perturbed pitchfork bifurcation as well (see Fig. 5).

As F_2 is decreased, all three branches undergo Hopf bifurcation for very small values of F_2. A decrease of the internal Rossby radius of deformation thus destabilizes the flow, as in Ghil et al.'s (2002b) two-mode QG model. The subpolar branch is destabilized for $F_2 = 0.20$ with a period of $T = 128$ days and the subtropical branch for $F_2 = 0.17$ with $T = 140$ days. Multiple equilibria disappear for $F_2 > 10.6$, leading to the existence of the subpolar branch of solutions only. An increase of the lower-layer thickness stabilizes the flow in the same way as in Dijkstra and Katsman's (1997) two-layer QG model. The flow patterns associated with the various branches and with the saddle-node bifurcation point at $F_2 = 10.6$ are shown in Fig. 5.

We computed Hopf bifurcations and saddle-node bifurcations with respect to σ as the depth H_2 of the lower

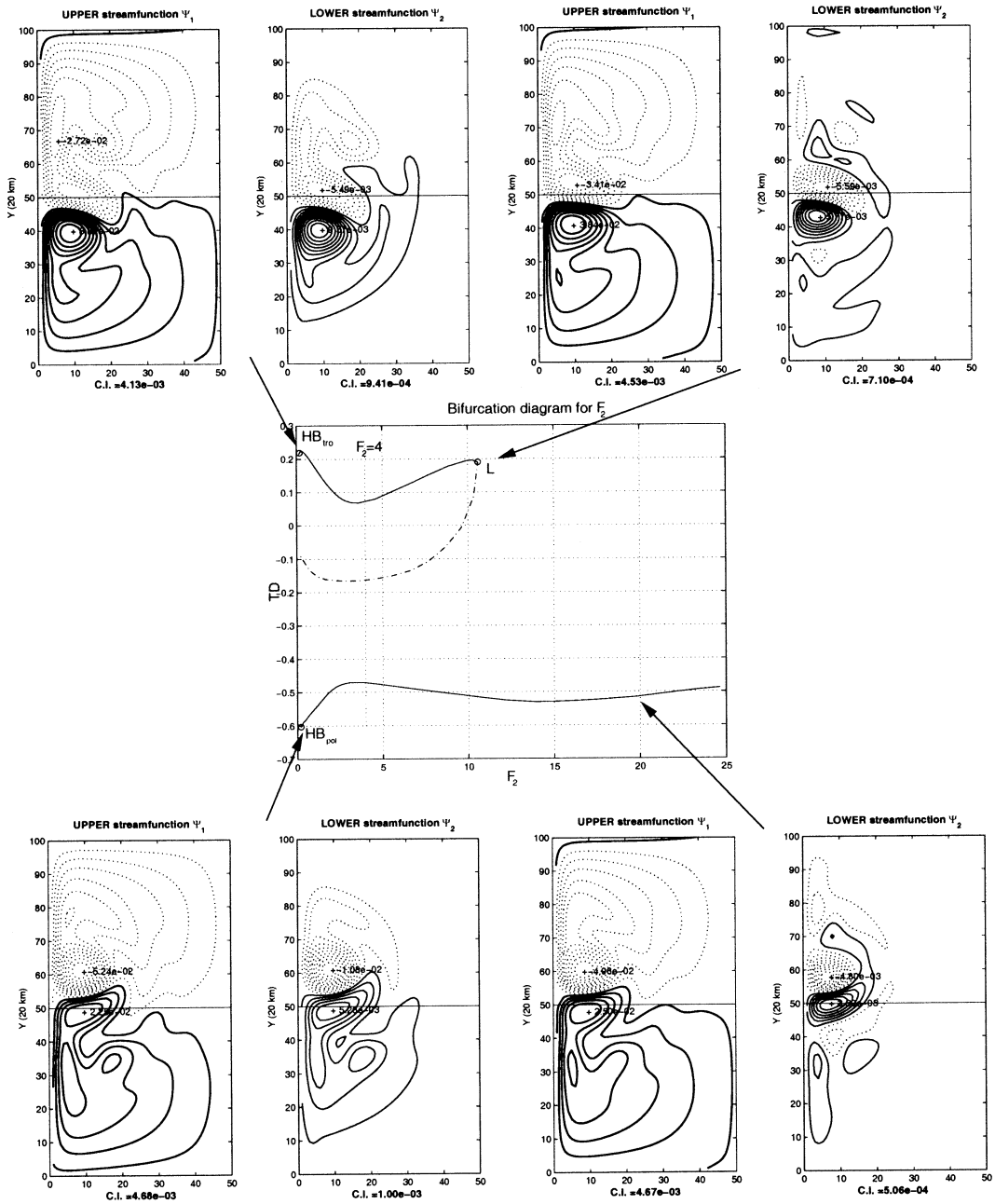

FIG. 5. Bifurcation diagram for the inverse Froude number F_2, with TD plotted vs F_2. The flow patterns are referred to the bifurcation diagram, as in Figs. 2 and 4: (lower right) the unique, subpolar branch for $F_2 = 20$; (upper right) the saddle-node bifurcation between the perturbed symmetric and the subtropical branch for $F_2 = 10.6$; $F_2 = 1$ on the subpolar (lower left) and subtropical (upper left) branch.

layer varies continuously. We compared two cases: in the upper panel of Fig. 6, the interface friction term is neglected, that is $\mu_1 = 0$, while in the lower one it is not.

When $\mu_1 = 0$, the active lower layer is motionless and stationary solutions do not depend on F_2; hence the solid line that marks the locus of the saddle-node bifurcation is vertical in the upper panel. For decreasing values of H_2, the disconnected branch of solutions becomes unstable in its entirety. The Hopf bifurcation off the subpolar branch occurs before the saddle-node bifurcation, as soon as $H_2 \leq 2050$ m. Subpolar-branch solutions are subject to oscillatory instability for small values of TD, when the asymmetry is weak. The period of the first unstable mode varies from 3 months for $H_2 = 50$ m to 5 months for larger values of H_2.

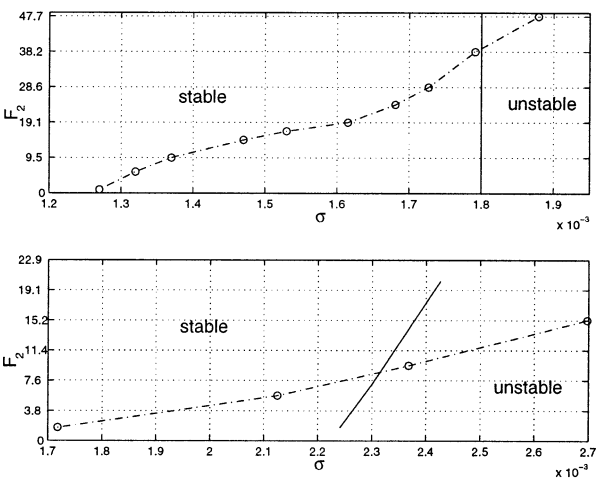

FIG. 6. Dependence of the Hopf bifurcation locus on the subpolar branch (dashed lines) and saddle-node bifurcation locus (solid line) on F_2: (top) $\mu_1 = 0$ and (bottom) $\mu_1 = 10^{-3}$. The values $g_1 = 3.82 \times 10^{-2}$ m s^{-2} and $g_2 = 1.91 \times 10^{-2}$ m s^{-2} of the reduced gravities and $H_1 = 500$ m, i.e., $F_1 = 19.10$, are held constant; all other parameter values are given in Table 1.

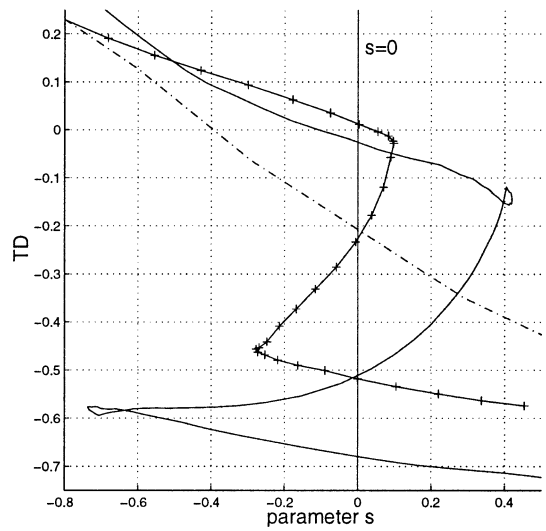

FIG. 7. Dependence on the zonal wind profile's asymmetry parameter s. The three bifurcations curves are for $\sigma = 1.27 \times 10^{-3}$ (dash–dotted line), $\sigma = 2.56 \times 10^{-3}$ (solid line marked by plus signs), and $\sigma = 3.51 \times 10^{-3}$ (plain solid line). Here $H_2 = 500$ m, i.e., $F_2 = 9.55$, while all other parameter values are as in Fig. 6.

In the lower panel of Fig. 6 we used a nonzero value of μ_1; that is, the upper and lower layer interact through the interface friction term. As we decrease H_2, the Hopf bifurcation occurs eventually before the saddle-node bifurcation as well. This, however, only happens for a much smaller H_2 value, of $H_2 = 450$ m, when compared with the value $H_2 = 2050$ m for $\mu_1 = 0$. For $\mu_1 \neq 0$, we obtained only a weak dependence of the first unstable mode's period as H_2 varies, with $T \simeq 4$ months over the entire range of H_2 values shown in the panel. Similar results were found by Dijkstra and Katsman (1997) for a two-layer QG model. Ghil et al. (2002b) also found a Hopf bifurcation before the pitchfork bifurcation for small enough values of the internal Rossby radius of deformation L_R in their two-mode model.

c. *Dependence on the asymmetry of the forcing*

We consider now a perturbation of the (anti-) symmetric profile of the wind stress forcing. The spatial pattern of the perturbation that we study is

$$\tau^x = -\tau_0 e^{s(y-D/2)} \cos(2\pi y/D); \tag{26}$$

τ^x/τ_0 is then normalized by its L_2 norm. For $s > 0$ the subpolar gyre is strengthened by the pumping of increased negative vorticity into its upper layer. The opposite is the case for $s < 0$; that is, the pumping of positive vorticity strengthens the subtropical gyre. Figure 7 shows the bifurcation diagrams with respect to the asymmetry parameter s, for three different values of the wind-stress intensity parameter σ.

For a small value of the wind-stress strength, $\sigma = 1.27 \times 10^{-3}$, only one solution exists over the entire range of s considered (dash–dotted line in the figure). As s decreases, the transport ratio TD in the figure increases and becomes positive. We obtain an antisymmetric solution with two gyres of equal strength for $s = -0.40$. This indicates that the existence of subpolar-branch solutions, with TD < 0, is quite robust to perturbations of the wind stress profile.

For σ large enough, multiple equilibria coexist. We obtain, for $\sigma = 2.56 \times 10^{-3}$ (line marked by plus signs), a connected, S-shaped curve that intersects the $s = 0$ axis three times. The solutions at $s = 0$ correspond to the subpolar-branch, subtropical-branch, and unstable-branch solutions in Fig. 2: these three branches are now connected through the wind stress profile's degree of asymmetry. The parameter s gives therewith a systematic and easy way to compute the isolated branch by starting from the subpolar branch and using continuation methods. Moreover, this method works well almost independently of the perturbation profile chosen. In Fig. 7, a fold develops for $\sigma \geq 3.4 \times 10^{-3}$ (plain solid line) near two values of the asymmetry parameter, $s = -0.64$ and $s = 0.40$.

d. *Dependence on the spatial resolution*

The western boundary currents' intensity and separation point have a substantial impact on the whole mid-latitude basin's double-gyre circulation. Given this impact, on the one hand, and these currents' sharp gradients, on the other, it is important to resolve the details of their boundary layer structure.

The frictional Munk layer has a nondimensional width $\delta_M = (A/\beta)^{1/3}/L$, while the corresponding inertial-layer width δ_I is proportional to $\epsilon^{1/2}$, where ϵ is the Rossby number (Pedlosky 1987, 1996; Chang et al. 2001: see sections 2a and 2b here for a definition of all

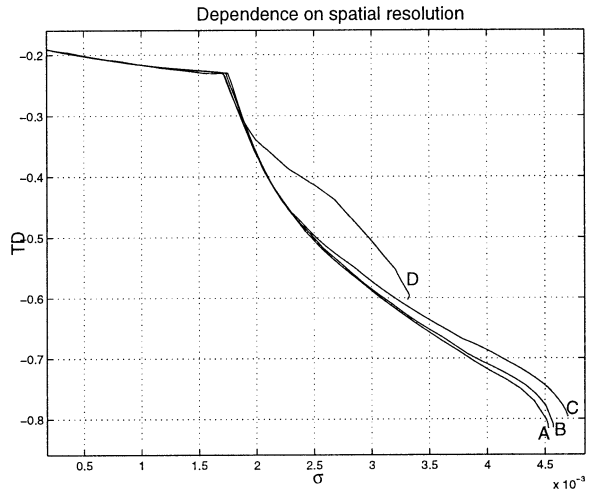

FIG. 8. Dependence of the bifurcation diagram on spatial resolution. The subpolar solution branch TD vs σ is shown for (A) 16.6 km, (B) 20 km, (C) 25 km, and (D) 33.3 km. Parameter values here are like in Fig. 6.

the intervening symbols). Typical values of these two nondimensional widths for midlatitude ocean flows are $0 < \delta_I \leq \delta_M \leq 0.1$ (Sheremet et al. 1997; Chang et al. 2001). Dimensional values, depending on the exact way that the location of each boundary layer's seaward limit is defined, are on the order of a few tens of kilometers. Moreover, it is not known a priori how many grid points are required to properly resolve the two overlapping boundary layers. We investigate therefore systematically the influence of the resolution on the bifurcation tree.

The influence of the grid size on the TD versus σ bifurcation diagram is studied first. We used four different grids with a spatial resolution of 33.3, 25, 20, and 16.6 km, respectively; Figs. 2–7 were obtained at a 20-km resolution. As the wind stress is increased from low values, the subpolar branch of solutions is the one that is chosen in every case (see Fig. 8). The difference between the curves obtained for all four resolutions is practically nil as long as $\sigma \leq 1.6 \times 10^{-3}$ that is, before the sudden drop in TD noted already in Fig. 2. The difference is still quite small up to $\sigma = 4.5 \times 10^{-3}$ for all but the coarsest mesh (curve D, $\Delta x = \Delta y = 33$ km). It is almost negligible over the entire range for curves A and B, that is, resolutions of 16.6 and 20 km.

Even when a different numerical scheme, like the Arakawa scheme (Arakawa and Lamb 1977), is used, the subpolar branch of solutions appears first (not shown). This property of the model is thus very robust, whatever the resolution and numerical discretization is.

The solutions with a spatially dominant subtropical gyre are preferred for values of the wind stress forcing that are quite realistic for a multilayer model. There is excellent agreement between all four curves in Fig. 8 up to $\sigma = 1.8 \times 10^{-3}$, that is, even beyond the drop in TD that selects the branch in the perturbed pitchfork bifurcation of Fig. 2. This agreement suggests that, in the weak wind stress forcing limit, the linear dynamics is mainly responsible for the choice of the branching structure. The choice in question is thus independent of using the Arakawa or the Lilly scheme, since the discretization of the nonlinear term is not important, and the detailed resolution of the western boundary layer is not very important either.

TABLE 2. Dependence of the first Hopf bifurcation on the horizontal resolution.

Mesh size	σ ($\times 10^{-3}$)	Period (days)
16.6	2.359	115.7
20.0	2.369	116.9
22.2	2.420	117.0
25.0	2.350	920.0 (spurious)

Dijkstra and Molemaker (1999), on the other hand, found a different branching structure for a 1½-layer SW model, in which the subtropical branch connected first, that is with $K^{\text{tro}} > K^{\text{pol}}$ instead of $K^{\text{tro}} < K^{\text{pol}}$ (see section 4b here). They used a different subgrid-scale parameterization of diffusion that is a velocity formulation $h\Delta u$ of the diffusive terms instead of our momentum formulation $\Delta(hu)$ and finite elements on an unstructured mesh. These authors also suggested that the effect of subgrid-scale parameterization could be important in explaining the choice of steady-state branch. We tested, therefore, the use of the velocity formulation as well. In our tests, however, it led to the same results (not shown) as in Fig. 8, with the subpolar branch connected first.

Shchepetkin and O'Brien (1996) discussed in considerable detail the effects of various lateral diffusion operators, including these two, for the SW equations. They showed that in the QG limit and for small deviations of the layers thickness, the velocity and momentum formulation of lateral diffusion are equivalent. The SW solutions we obtained up to this point indicate the relative smallness of the thickness deviations, whose largest value at the center of the strongest recirculation cell is always less than 10% of the total thickness of the two active layers. In the limit of zero wind stress forcing, the deviations of both layers from uniform thickness are much smaller, so different subgrid-scale parameterizations should lead to the same choice of the solution branch. This point may be important since, as Part II indicates, the branch that is connected to low wind stress forcing is the one that plays a major role in the low-frequency variability of the aperiodic solutions.

We also computed the first Hopf bifurcation off the subpolar branch, corresponding to the cases A, B, and C in Fig. 8 as well as to an additional resolution of 22.2 km. The results of these computations are summarized in Table 2.

Although the 25-km resolution gives good results when considering stationary solutions only, the table indicates that it is not sufficient to capture correctly the

first Hopf bifurcation: a spurious mode with a much longer period appears before the expected mode. The 20-km resolution seems to be rather close to convergence and thus a good compromise. We will see in Part II that this resolution suffices even to capture the phenomenology of strongly nonlinear, highly unsteady flows past the first Hopf bifurcation.

6. Summary

Numerical bifurcation tools have enabled us to determine the multiplicity and stability of equilibrium solutions of a 2½-layer SW model for the double-gyre, wind-driven ocean circulation in a rectangular midlatitude basin. The model is sketched in Fig. 1 and governed by Eqs. (4). The boundary conditions and zonal-wind profile are symmetric about the domain's E–W axis. As one increases the intensity σ of the zonal wind stress, while keeping its meridional profile symmetric about the rectangle's center line, the double-gyre circulation undergoes a perturbed pitchfork bifurcation.

As a result, multiple steady-state solutions coexist for a sufficiently strong forcing: an almost antisymmetric solution with two gyres of nearly equal strength is unstable, while two asymmetric solutions are stable for the same value of σ (see Fig. 2). One of the two has a stronger cyclonic subpolar gyre. This branch of steady-state solutions, which we call therefore subpolar, has a more extensive subtropical gyre, as found in all midlatitude ocean basins. The other asymmetric solution can be obtained approximately from the subpolar-branch solution by mirror symmetry in the basin's E–W axis. It has a stronger anticyclonic recirculation cell, a more extensive subpolar gyre, and forms what we call the subtropical branch of solutions.

On all three branches, the two western boundary currents merge to form a meandering eastward jet as they separate from the boundary. In the inertial recirculation zone near the separation points, a vigorous dipole is formed by two counterrotating vortices, anticyclonic and cyclonic. The relative strength of the two localized concentrations of potential vorticity (see section 2b), negative and positive, differs from one branch to another and also between the two active layers.

As the system's nonlinearity increases, the second active layer interacts more and more through interface friction with the first layer. The western boundary currents, where the flow velocity is largest, as well as the strong dipolar recirculation zone, act on the more quiescent lower layer. For even stronger forcing, each branch of solutions undergoes a Hopf bifurcation that leads to solutions with stable periodic behavior.

This behavior is very robust to changes in a number of parameters, such as interfacial friction, lower-layer thickness, and spatial resolution. Changing gradually the meridional wind-stress profile from symmetric to more and more asymmetric does not change the structure of the bifurcation diagram. Under all the circumstances tested, the flow pattern that has a spatially dominant subtropical gyre is preferred. In this pattern, the separation point of the western boundary currents lies poleward of the symmetry axis and the detached eastward jet runs northeastward.

In Part II we will describe in greater detail the structure of the unstable modes and the dynamics that leads to chaotic behavior. The nature of the associated low-frequency variability will be described for both rectangular geometry and a more realistic geometry that resembles the North Atlantic basin.

Acknowledgments. It is a pleasure to thank H. A. Dijkstra, S. Jiang, and S. Speich for discussions and correspondence. The work of ES was supported by a doctoral fellowship at the Université Paris-Sud, while MG's work was supported by an NSF Special Creativity Award and NSF Grant ATM00-82131, and KI's by ONR Grant N00014-99-109920. Computations were carried out at Indiana University and IDRIS (France) with support from NSF Grant CDA-9601632 (RT). Author SW is supported in part by the Office of Naval Research under Grant N00014-96-1-0425 and by the National Science Foundation under Grant DMS-0072612.

REFERENCES

Arakawa, A., and V. R. Lamb, 1977: Computational design of the basic dynamical processes of the UCLA general circulation model. *Methods in Computational Physics*, J. Chang, Ed., Vol. 17, Academic Press, 173–265.

Berloff, P. S., and S. P. Meacham, 1997: The dynamics of an equivalent-barotropic model of the wind-driven circulation. *J. Mar. Res.,* **55,** 407–451.

——, and ——, 1998: The dynamics of a simple baroclinic model of the wind-driven circulation. *J. Phys. Oceanogr.,* **28,** 361–388.

Broomhead, D. S., and G. P. King, 1986: Extracting qualitative dynamics from experimental data. *Physica D,* **20,** 217–236.

Bryan, K., 1963: A numerical investigation of a nonlinear model of a wind-driven ocean. *J. Atmos. Sci.,* **20,** 594–606.

Buffoni, G., and A. Griffa, 1990: The finite-difference barotropic vorticity equation in ocean circulation modelling: Basic properties of the solutions. *Dyn. Atmos. Oceans,* **15,** 1–32.

Cessi, P., and G. R. Ierley, 1995: Symmetry-breaking multiple equilibria in quasigeostrophic, wind-driven flows. *J. Phys. Oceanogr.,* **25,** 1196–1202.

Chang, K. I., K. Ide, M. Ghil, and C.-C. A. Lai, 2001: Transition to aperiodic variability in a wind-driven double-gyre circulation model. *J. Phys. Oceanogr.,* **31,** 1260–1286.

Chassignet, E. P., and P. R. Gent, 1991: The influence of boundary conditions on midlatitude jet separation in ocean numerical models. *J. Phys. Oceanogr.,* **21,** 1290–1299.

Christodoulou, K. N., and L. E. Scriven, 1988: Finding leading modes of a viscous free surface flow: An asymmetric generalized eigenproblem. *J. Sci. Comput.,* **3,** 335–406.

Colebrook, J. M., 1978: Continuous plankton records: zooplankton and environment, Northeast Atlantic and North Sea. *Oceanol. Acta,* **1,** 9–23.

Davis, T. A., and I. S. Duff, 1997: An unsymmetric-pattern multifrontal method for sparse LU factorization. *SIAM J. Matrix Anal. Appl.,* **18,** No. 1, 140–158.

Dettinger, M. D., M. Ghil, C. M. Strong, W. Weibel, and P. Yiou, 1995: Software expedites singular-spectrum analysis of noisy time series. *Eos., Trans. Amer. Geophys. Union,* **76,** 12–21.

Dijkstra, H. A., and C. A. Katsman, 1997: Temporal variability of

the wind-driven quasigeostrophic double gyre ocean circulation: Basic bifurcation diagrams. *Geophys. Astrophys. Fluid Dyn.,* **85,** 195–232.

——, and M. J. Molemaker, 1999: Imperfections of the North-Atlantic wind-driven ocean circulation: Continental geometry and asymmetric windstress. *J. Mar. Res.,* **57,** 1–28.

Dowling, T. E., 1995: Dynamics of Jovian atmospheres. *Annu. Rev. Fluid. Mech.,* **27,** 293–334.

Fraedrich, K., 1986: Estimating the dimensions of weather and climate attractors. *J. Atmos. Sci.,* **43,** 419–432.

Ghil, M., and S. Childress, 1987: *Topics in Geophysical Fluid Dynamics: Atmospheric Dynamics, Dynamo Theory and Climate Dynamics.* Springer-Verlag, 485 pp.

——, and A. W. Robertson, 2000: Solving problems with GCMs: General circulation models and their role in the climate modeling hierarchy. *General Circulation Model Development: Past, Present and Future,* D. Randall, Ed., Academic Press, 285–325.

——, and Coauthors, 2002a: Advanced spectral methods for climatic time series. *Rev. Geophys.,* **40,** 1003, doi:10.1029/2000RG000092.

——, Y. Feliks, and L. Sushama, 2002b: Baroclinic and barotropic aspects of the wind-driven double-gyre circulation. *Physica D,* **167,** 1–35.

Gill, A. E., 1982: *Atmosphere–Ocean Dynamics.* Academic Press, 662 pp.

Golub, G. H., and C. F. Van Loan, 1996: *Matrix Computations.* 3d ed. The Johns Hopkins University Press, 642 pp.

Grammeltvedt, A., 1969: A survey of finite-difference schemes for the primitive equations for a barotropic fluid. *Mon. Wea. Rev.,* **97,** 384–404.

Hellerman, S., and M. Rosenstein, 1983: Normal monthly wind stress over the world ocean with error estimates. *J. Phys. Oceanogr.,* **13,** 1093–1104.

Jiang, S., and M. Ghil, 1993: Dynamical properties of error statistics in a shallow-water model. *J. Phys. Oceanogr.,* **23,** 2541–2566.

——, and M. Ghil, 1997: Tracking nonlinear solutions with simulated altimetric data in a shallow-water model. *J. Phys. Oceanogr.,* **27,** 72–95.

——, F. F. Jin, and M. Ghil, 1993: The nonlinear behavior of western boundary currents in a wind-driven, double-gyre, shallow-water model. Preprints, *Ninth Conf. on Atmospheric and Oceanic Waves and Stability,* San Antonio, TX, Amer. Meteor. Soc., 64–67.

——, ——, and ——, 1995: Multiple equilibria, periodic, and aperiodic solutions in a wind-driven, double-gyre, shallow-water model. *J. Phys. Oceanogr.,* **25,** 764–786.

Keller, H. B., 1977: Numerical solution of bifurcation and nonlinear eigenvalue problems. *Applications of Bifurcation Theory,* P.H. Rabinowitz, Ed., Academic Press, 359–384.

Keppenne, C. L., S. Marcus, M. Kimoto, and M. Ghil, 2000: Intraseasonal variability in a two-layer model and observations. *J. Atmos. Sci.,* **57,** 1010–1028.

Kubiček, M., and M. Marek, 1983: *Computational Methods in Bifurcation Theory and Dissipative Structures.* Springer-Verlag, 243 pp.

Legras, B., and M. Ghil, 1985: Persistent anomalies, blocking and variations in atmospheric predictability. *J. Atmos. Sci.,* **42,** 433–471.

McCalpin, J., and D. Haidvogel, 1996: Phenomenology of the low-frequency variability in a reduced-gravity, quasi-geostrophic double-gyre model. *J. Phys. Oceanogr.,* **26,** 739–752.

Meacham, S. P., 2000: Low-frequency variability in the wind-driven circulation. *J. Phys. Oceanogr.,* **30,** 269–293.

——, and P. S. Berloff, 1997: Instabilities of a steady, barotropic, wind-driven circulation. *J. Mar. Res.,* **55,** 885–913.

Miller, A. J., W. R. Holland, and M. C. Hendershott, 1987: Open-ocean response and normal mode excitation in an eddy-resolving general circulation model. *Geophys. Astrophys. Fluid Dyn.,* **37,** 253–278.

Nauw, J. J., and H. A. Dijkstra, 2001: The origin of low-frequency variability of double-gyre wind-driven flows. *J. Mar. Res.,* **59,** 567–597.

Pedlosky, J., 1987: *Geophysical Fluid Dynamics.* 2d ed. Springer-Verlag, 710 pp.

——, 1996: *Ocean Circulation Theory.* Springer-Verlag, 453 pp.

Primeau, F. W., 1998: Multiple equilibria of a double-gyre ocean model with super-slip boundary conditions. *J. Phys. Oceanogr.,* **28,** 2130–2147.

Seydel, R., 1994: *Practical Bifurcation and Stability Analysis: From Equilibrium to Chaos.* Springer-Verlag, 407 pp.

Shchepetkin, A., and J. J. O'Brien, 1996: A physically consistent formulation of lateral friction in shallow-water equation ocean models. *Mon. Wea. Rev.,* **124,** 1285–1300.

Sheremet, V. A., G. R. Ierley, and V. M. Kamenkovitch, 1997: Eigenanalysis of the two-dimensional wind-driven ocean circulation problem. *J. Mar. Res.,* **55,** 57–92.

Simonnet, E., 1998: Some numerical problems related to geophysical flows. Ph.D. thesis, Université de Paris-Sud, Orsay, France, 154 pp.

——, and H. A. Dijkstra, 2002: Spontaneous generation of low-frequency modes of variability in the wind-driven ocean circulation. *J. Phys. Oceanogr.,* **32,** 1747–1762.

——, R. Temam, S. Wang, M. Ghil, and K. Ide, 1998: Successive bifurcations in a shallow-water ocean model. *Sixteenth International Conference on Numerical Methods in Fluid Dynamics,* C.-H. Bruneau, Ed., *Lecture Notes in Physics,* Vol. 515, Springer-Verlag, 225–230.

——, M. Ghil, K. Ide, R. Temam, and S. Wang, 2003: Low-frequency variability in shallow-water models of the wind-driven ocean circulation. Part II: Time-dependent solutions. *J. Phys. Oceanogr.,* **33,** 729–752.

Speich, S., and M. Ghil, 1994: Interannual variability of the mid-latitude oceans: A new source of climate variability? *Sistema Terra,* **3** (3), 33–35.

——, H. A. Dijkstra, and M. Ghil, 1995: Successive bifurcations in a shallow-water model applied to the wind-driven ocean circulation. *Nonlinear Proc. Geophys.,* **2,** 241–268.

Stewart, W. J., and A. Jennings, 1981: A simultaneous iteration algorithm for real matrices. *ACM Trans. Math. Software,* **7,** 184–198.

Stommel, H., 1948: The westward intensification of wind-driven ocean currents. *Trans. Amer. Geophys. Union,* **29,** 202–206.

Temam, R., 1998: *Infinite-Dimensional Dynamical Systems in Mechanics and Physics.* 2d ed. Springer-Verlag, 500 pp.

Vautard, R., and M. Ghil, 1989: Singular spectrum analysis in nonlinear dynamics, with applications to paleoclimatic time series. *Physica D,* **35,** 395–424.

Veronis, G., 1963: An analysis of wind-driven ocean circulation with a limited number of Fourier components. *J. Atmos. Sci.,* **20,** 577–593.

——, 1966: Wind-driven ocean circulation. II: Numerical solution of the nonlinear problem. *Deep-Sea Res.,* **13,** 31–55.

Verron, J., and C. Le Provost, 1978: Wind-driven ocean circulation transition to barotropic instability. *Dyn. Atmos. Oceans,* **11,** 175–201.

Wang, S., 1992: Attractors for the 3D baroclinic quasi-geostrophic equations of large-scale atmosphere. *J. Math. Anal. Appl.,* **165,** 266–283.

Wolanski, G., 1989: The barotropic vorticity equation under forcing and dissipation: Bifurcations of nonsymmetric responses and multiplicity of solutions. *SIAM J. Appl. Math.,* **49,** 1585–1607.

——, and M. Ghil, 1995: Stability of quasi-geostrophic flow in a periodic channel. *Phys. Lett.,* **202A,** 111–116.

——, and ——, 1996: An extension of Arnol'd's second stability theorem for the Euler equations. *Physica D,* **94,** 161–167.

——, and ——, 1998: Nonlinear stability for saddle solutions of ideal flows and symmetry breaking. *Commun. Math. Physics,* **193,** 713–736.